Heliyon 10 (2024) e35502

Contents lists available at ScienceDirect

Heliyon

journal homepage: www.cell.com/heliyon

Research article

Noninvasive assessment of liver fibrosis in mini pigs using an ^{18}F–AlF-NOTA-RGD2 PET/CT molecular probe

Wenrui Liu [a,1], Hongwei Xu [b,1], Haili Zhang [b,1], Maodi Xie [c], Yundi Liu [a], Li Wang [e], Xiaoai Wu [d,**], Yinrui Feng [a,***], Kefei Chen [a,b,*]

[a] Regenerative Medicine Research Center, Sichuan University West China Hospital, Chengdu, Sichuan, 610041, China
[b] Department of Liver Surgery, Center of Liver Transplantation, West China Hospital, Sichuan University, Chengdu, Sichuan, 610041, China
[c] Laboratory of Mitochondria and Metabolis, Wmest China Hospital, Sichuan University, Chengdu, Sichuan, 610041, China
[d] Department of Nuclear Medicine, Laboratory of Clinical Nuclear Medicine, West China Hospital, Sichuan University, Chengdu, Sichuan, 610041, China
[e] Jiangsu Xinrui Pharmaceutical Co., Ltd, Jiangsu, 226500, China

ARTICLE INFO

Keywords:
Molecular probe
Liver fibrosis
Diagnostic imaging
Noninvasive method
Mitochondrial function

ABSTRACT

To evaluate the efficacy of the 18F–AlF-NOTA-RGD2 positron emission tomography (PET)/computed tomography (CT) molecular probe for the noninvasive staging of liver fibrosis in mini pigs, a potential alternative to invasive diagnostic methods was revealed. This study used 18F–AlF-NOTA-RGD2 PET/CT imaging of mini pigs to assess liver fibrosis. The methods included synthesis and quality control of the molecular probe, establishment of an animal model of liver fibrosis, blood serum enzymatic tests, histopathological examination, PET/CT imaging, collagen content and expression, and mitochondrial reserve function assessment. The 18F–AlF-NOTA-RGD2 PET/CT molecular probe effectively differentiated various stages of liver fibrosis in mini pigs. Blood serum enzymatic tests revealed distinct stages of liver fibrosis, revealing significant increases in AST, ALT, TBIL, and DBIL levels as fibrosis advanced. Notably, ALT levels increased markedly in severe fibrosis patients. A gradual increase in collagen deposition and increasing α-SMA RNA expression and protein levels effectively differentiated between mild and severe fibrosis stages. Pathological examinations and Sirius Red staining confirmed these findings, highlighting substantial increases in collagen accumulation. PET/CT imaging results aligned with histopathological findings, showing that increased radiotracer uptake correlated with fibrosis severity. Assessments of mitochondrial function revealed a decrease in total liver glutathione content and mitochondrial reserve capacity, especially in patients with severe fibrosis. The

Abbreviations: **PET**, Positron emission tomography; **CT**, Computed tomography; **GSH**, Glutathione; **AST**, Aspartate transaminase; **ALT**, Alanine transaminase; **TBIL**, Total bilirubin; **DBIL**, Direct bilirubin; **ALP**, Alkaline phosphatase; **ALB**, Albumin; **HE**, Hematoxylin and eosin; **HYP**, Hydroxyproline; **GSSG**, Oxidized glutathione disulfide; **HPLC**, High-performance liquid chromatography; **BDL**, Bile duct ligation; **ROI**, Region of interest.

** Corresponding author. Department of Liver Surgery, Center of Liver Transplantation, West China Hospital, Sichuan University, Chengdu, Sichuan, 610041, China
*** Corresponding author. Regenerative Medicine Research Center, Sichuan University West China Hospital, Chengdu, Sichuan, 610041, China
* Corresponding author. Department of Liver Surgery, Center of Liver Transplantation, West China Hospital, Sichuan University, Chengdu, Sichuan, 610041, China
E-mail addresses: xiaoai.wu@scu.edu.cn (X. Wu), rayinfeng@163.com (Y. Feng), ckf2003@163.com (K. Chen).
[1] These authors contributed equally to the work.

https://doi.org/10.1016/j.heliyon.2024.e35502
Received 5 March 2024; Received in revised form 30 July 2024; Accepted 30 July 2024
Available online 31 July 2024

18F–AlF-NOTA-RGD2 PET/CT molecular probe is a promising tool for the noninvasive assessment of liver fibrosis, offering potential benefits over traditional diagnostic methods in hepatology.

1. Introduction

Liver fibrosis, resulting from chronic liver injury, leads to progressive scarring and is a critical step toward cirrhosis and hepatocellular carcinoma development [1,2]. Traditionally, liver fibrosis is staged through liver biopsies [3]. Despite being the standard, this invasive approach carries risks such as complications and sampling errors, underscoring the need for safer, noninvasive diagnostic methods [1,4,5].

The emergence of molecular imaging, especially with the use of specific molecular probes in positron emission tomography (PET)/computed tomography (CT), has revolutionized the noninvasive assessment of liver conditions [6,7]. The 18F–AlF-NOTA-RGD2 PET/CT molecular probe is particularly notable for its affinity for integrin αvβ3, a protein that is significantly expressed in activated hepatic stellate cells and plays a key role in fibrogenesis [6,8]. The RGD motif, which is crucial for integrin targeting, enhances the probe's specificity, making it a promising tool for liver fibrosis imaging [9,10].

Treating liver fibrosis presents significant challenges and often requires surgical intervention [11]. Most liver resections are performed against a background of fibrosis, where postoperative liver function becomes a paramount concern [11]. The diminishing reserve capacity of the liver as fibrosis progresses underscores the urgency for precise, noninvasive diagnostic techniques to assess liver function pre- and postsurgery [12,13]. These new methods are vital for optimizing surgical outcomes, reducing postoperative complications, and lowering liver failure mortality rates.

Our study utilized the 18F–AlF-NOTA-RGD2 PET/CT molecular probe to evaluate liver fibrosis in mini pigs, an animal model closely mimicking human physiology, thereby providing a relevant platform for human liver disease studies [14–16]. This research aimed to validate the accuracy of the probe for fibrosis staging and compare its effectiveness with that of traditional diagnostic methods, such as histopathology and serum marker detection. Furthermore, we aimed to confirm whether this noninvasive approach can reliably reflect liver function, which is essential for its adoption in clinical decision-making surrounding liver surgeries.

In summary, our study sought to affirm the diagnostic value of the 18F–AlF-NOTA-RGD2 PET/CT probe in liver fibrosis, exploring its potential to transform current practices by offering a safer, more patient-friendly alternative for disease management and monitoring.

2. Materials and methods

2.1. Materials

18F-fluoride with no carrier added was obtained from Jiangsu Xinrui Pharmaceutical (Jiangsu, China). 18F-FDG was purchased from Jiangsu Xinrui Pharmaceutical (Jiangsu, China). The peptides pegylated into dimeric RGD peptides PEG3-E[c(RGDyK)]2 (denoted as PRGD2) and NOTA-PRGD2 were synthesized by Jiangsu Xinrui Pharmaceutical (Jiangsu, China). Mini pigs (28–30 weeks old) were purchased from Sichuang Western Hospital Experimental Animal Center (Chengdu, China). A Sirius Red Staining Kit was purchased from Abcam (Cambridge, UK). Hydroxyproline (HYP), glutathione (GSH) and oxidized glutathione disulfide (GSSG) were purchased from the Jiancheng Institute of Biotechnology (Nanjing, China).

2.2. Synthesis and quality control of the 18F–AlF-NOTA-RGD2PET/CT molecular probe

The synthesis of the 18F–AlF-NOTA-RGD2 PET/CT probe was conducted according to a previously reported protocol [17]. In brief, 3 μL of aluminum chloride (2 mM) in 0.2 M sodium acetate buffer at pH = 4 was added to 0.1 mL of aqueous [18F] fluoride (0.37 GBq) in a 1.0 mL V-vial. The resulting solution was heated at 100 °C for 10 min to generate the aluminum–fluoride complex. After the vial was cooled, 6 μL of NOTA-PRGD2 (2 mM) in 0.2 M sodium acetate buffer at pH 4 was added. Subsequently, the vial was heated at 100 °C for an additional 10 min. After the reaction finished, the mixture was directly applied to a C18 cartridge, bypassing high-performance liquid chromatography (HPLC) purification, and then eluted with 0.3 mL of 80 % ethanol/water containing 2 % acetic acid. The ethanol in the solution was evaporated using an argon flow, and the resulting product was diluted in PBS for further studies.

The radio-chemical purity of 18F–AlF-NOTA-RGD2 was measured on an Agilent 1100 HPLC instrument equipped with an FC3200 gamma detector (Eckert & Ziegler). An Agilent ZORBAX SB-C18 column (4.6 × 250 mm, 5 μm) was used to analyze the final product on the HPLC system under the following conditions: 1. Mobile phase A: acetonitrile, mobile phase B: 0.1 % trifluoroacetic acid in H2O; 2. Flow rate: 1 mL/min; 3. For the gradient, see Table S1. The HPLC chromatogram of 18F–AlF-NOTA-RGD2 is presented in Fig. S1, which indicates that the radiochemical purity of 18F–AlF-NOTA-RGD2 was greater than 99 %, with a retention time of 25.45 min.

2.3. Animal model

All procedures for animal care and experimental operation were approved by the Institutional Animal Care and Use Committee (IACUC) of Sichuan University West China Hospital following the guidelines of the US National Institutes of Health (approval no.

20231023004). An animal model of liver fibrosis was established through the application of common bile duct ligation (BDL). Six-month-old male mini pigs were anesthetized using the ShuTai method. Following satisfactory anesthesia, a midline laparotomy was performed, and a transverse incision was made at the site of the common bile duct.

2.4. ^{18}F–AlF-NOTA-RGD2 PET/CT imaging

Dynamic PET/CT scans at different stages of liver fibrosis were performed for 1 h on a Biograph mCT scanner (Siemens). Briefly, the pigs were fasted for at least 6 h prior to the procedure to optimize the imaging conditions. Following anesthesia, ^{18}F–AlF-NOTA-RGD2 was administered intravenously, and PET/CT scans were conducted at specific time points postinjection to obtain optimal imaging data.

2.5. Blood serum enzymatic tests

Blood samples were collected from the submandibular vein plexus prior to the pigs being euthanized. Serum alanine aminotransferase (ALT), aspartate aminotransferase (AST), total bilirubin (TBIL), direct bilirubin (DBIL), alkaline phosphatase (ALP) and albumin (ALB) levels were measured using an automatic biochemical analyzer (COBAS 6000 C501, Roche Diagnostics).

2.6. Histopathological examination

Liver tissues were fixed in a 10 % neutral formalin solution, dehydrated and embedded in paraffin. The dehydration process involved gradient ethanol, and subsequent paraffin embedding was performed. Sections were then stained with hematoxylin and eosin (HE) or picrosirius red following previously reported methods [18].

2.7. Pathological staging

Pathology of the liver was conducted on tissue samples. All sections were scored (double-read) based on the METAVIR system [19]. The pigs were categorized into five groups: F0, indicating no fibrosis; F1, indicating mild fibrosis characterized by portal fibrosis without septa; F2, representing moderate fibrosis with few septa; F3, denoting severe fibrosis with numerous septa but no cirrhosis; and F4, indicating cirrhosis. Pigs without fibrosis were sourced from the control group. F1 and F2 were classified as mild fibrosis, while F3 and F4 were classified as severe fibrosis.

2.8. Sirius red staining

Collagen deposition in liver tissues was evaluated with Sirius red staining, which was performed according to the instructions of the Sirius Red Staining Kit. Quantitative analysis was conducted on five randomly selected fields from each slice using ImageJ for visualization and measurement.

2.9. PET/CT imaging operation and quantification

The dynamic PET data consisting of 17 images were reconstructed with durations of 15, 15, 15, 15, 30, 30, 30, 30, 60, 60, 60, 120, 120, 300, 300, 300, and 300 s. Each image was represented by a matrix with a pixel size of 0.95 mm and a fixed slice thickness of 0.8 mm using a two-dimensional ordered subset expectation imization (OSEM2D) protocol with four iterations. Dynamic PET images were analyzed to obtain multiple numeric kinetic data. Regions of interest (ROIs) were manually selected for plotting liver areas at different times. The SUV was calculated for regions of interest (ROIs) to quantify radiotracer uptake. Given a tissue density of 1 g/cm3, these values were subsequently normalized by the injected activity, yielding an image-derived mean ROI and the maximum percentage of injected dose per gram of body weight (%ID/g).

2.10. Hydroxyproline assay

Hepatic HYP was measured by a commercial kit according to the manufacturer's instructions.

2.11. Reverse transcription and qRT–PCR

Total RNA was extracted using a commercial kit (Aidlab, China) following the manufacturer's instructions. The concentration of total RNA was quantified using a NanoDrop 2000 spectrophotometer (Thermo Fisher, USA). cDNA was synthesized by reverse transcribing 1 μg of RNA using a Prime Script RT reagent kit (RR037A, TaKaRa). cDNA was amplified using SYBR Premix Ex *Taq*II (TaKaRa) with primers for a-SMA (forward primer 5′- ACTTCCAGTACGGTCTCCC-3′, reverse primer 5′- AGTCTCTGACATCCGCCCTA-3′). β-Actin (forward primer 5′- CCTCACTGTCCACCTTCC -3′, reverse primer 5′- GGGTGTAAAACGCAGCTC -3′) served as a loading control.

2.12. Western blotting analysis

Total proteins were extracted using a commercial kit (Aidlab, China) following the manufacturer's instructions. The protein concentrations were determined by a BCA protein assay kit (Thermo). Equal amounts of protein (20 μg) were separated by SDS–PAGE and transferred to a polyvinylidene fluoride membrane (Bio-Rad). The membranes were blocked in 5 % nonfat milk for 1 h at 37 °C and then incubated with primary antibodies (rat anti-SMA, 1:1000, ABclonal; rat anti-Integrin αV, 1:500, ABclonal; rat anti-Integrin β3, 1:500, ABclonal) overnight at 4 °C and HRP-conjugated goat anti-rabbit secondary antibodies (AC026, ABclonal) for 1 h at 37 °C. The blot was visualized using a chemiluminescence HRP substrate (Millipore) and analyzed by FusionCapt Advance software.

2.13. Immunohistochemical staining

Some sections were deparaffinized in easy tissue clearant and rehydrated in gradient alcohol followed by 3 % hydrogen peroxide treatment. The tissue sections were then incubated overnight with a primary antibody (rat anti-αv, rat anti-β3) (ABclonal) at 4 °C and

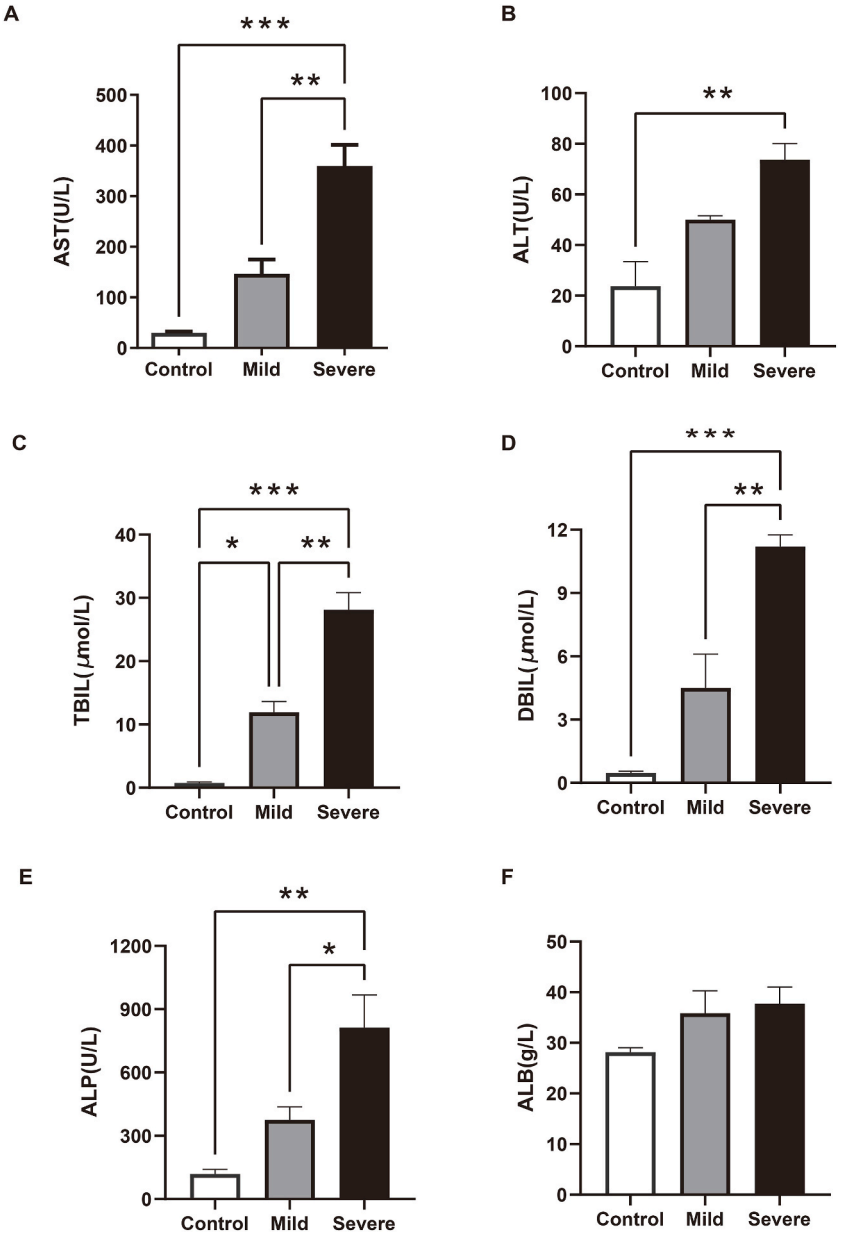

Fig. 1. Serum indicators of liver fibrosis. (A) Serum ALT, (B) AST, (C) TBIL, (D) DBIL, (E) ALP and (F) ALB concentrations. The data are expressed as the mean ± standard error (SEM) (n = 3 for each group). *P < 0.05, **P < 0.01, ***P < 0.001.

subsequently incubated with an HRP-labeled goat anti-rabbit secondary antibody (Cell Signaling Technology) at 37 °C for 1 h. Finally, the sections were processed with a freshly mixed diaminobenzidine kit according to the manufacturer's instructions, and the nuclei were counterstained with hematoxylin. Three to five visual fields of each sample were randomly selected and collected with a

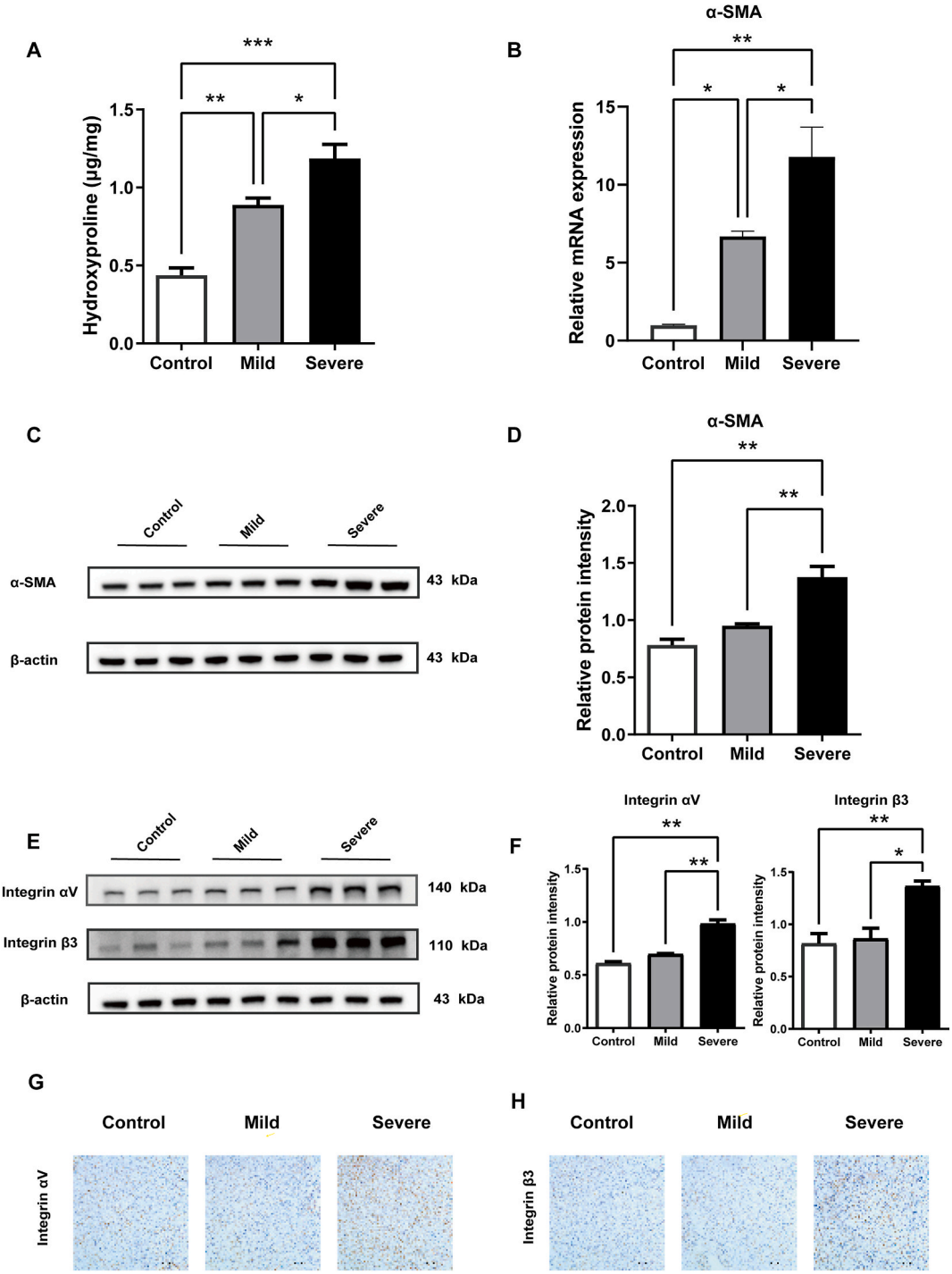

Fig. 2. Collagen content and expression. (A) Hepatic hydroxyproline. (B) The mRNA levels of α-SMA. (C) The protein levels of α-SMA and (D) its quantification by Western blot. β-actin served as a loading control. (E) The protein levels of integrin αV and integrin β3 and (F) its quantification by Western blot. β-actin served as a loading control. (G) Immunohistochemical staining of αV positive cells (brown) and (H) β3-positive cells (brown) in the liver. Scale bar = 50 μm. The data are expressed as the mean ± standard error (SEM) (n = 3 for each group). *P < 0.05, **P < 0.01, ***P < 0.001.

microscope (Eclipse 80i, Nikon) and analyzed by ImageJ software.

2.14. APRI calculation

The APRI was calculated as the APRI = [AST (IU/L)/upper limit of normal] × 100/PLT (10^9/L).

2.15. Glutathione assay

Hepatic GSH and GSSG were measured by a commercial kit according to the manufacturer's instructions.

2.16. Assessment of mitochondrial reserve function

Tissue samples (100 mg) from pigs with varying degrees of liver fibrosis were immediately obtained and placed in a dish containing PBS. Within a clean bench, the liver fascia was removed, and the liver tissue was shredded, followed by the addition of 10 mL of digestion fluid. The mixture was then oscillated at 37 °C for approximately 10 min for digestion. The suspension was filtered through a 70-75-μm membrane and a Dual Mfg filter. Then, 50 g of the filtrate was centrifuged at 4 °C for 3 min, after which the supernatant was discarded. The pellet was washed three times with DMEM containing 10 % FBS, each at 1000 rpm and 4 °C, for 5 min. Finally, the cells were resuspended in 5 mL of DMEM containing 5 % FBS. After assessing cell viability with 10 μl of the cell suspension, primary cells were seeded on an XF24 cell plate. The plate was then filled with analysis detection liquid containing 2 mM glutamine, 10 mM glucose, and 1 mM pyruvate. Oligomycin, FCCP, and antimycin combined with rotenone were sequentially injected to final concentrations of 5 μM, 3 μM, and 1 μM, respectively. The cellular oxygen consumption rate was measured using a Seahorse XFp Analyzer, and OCRs were measured as pmol s^{-1} mg^{-1} tissue weight [20].

2.17. Statistical analysis

All the data were analyzed using GraphPad Prism 9.0 and are presented as the mean ± SEM. ANOVA was used to compare continuous variables. Comparisons between groups were made using one-way analysis with Tukey's multiple comparisons test. The level of significance was considered at $P < 0.05$.

3. Results

3.1. Serum indicators of liver fibrosis

Following bile duct ligation, we conducted routine hepatic fibrosis tests on mini pig blood samples at various time points. Combined analysis of the AST, ALT, TBIL, and DBIL levels revealed that disease progression occurred in three stages: preoperative normal, mild fibrosis, and severe fibrosis (Fig. 1A–D). AST, DBIL, TBIL and ALP significantly increased with increasing degrees of fibrosis (Fig. 1A–C-E). Significant differences in ALT levels were observed between normal controls and pigs with severe fibrosis (Fig. 1B), while serum ALB levels varied across stages but were not significantly different (Fig. 1F).

3.2. Collagen content and expression

The hydroxyproline results indicated that collagen deposition gradually increased with the progression of fibrosis (Fig. 2A). Correspondingly, the RNA expression levels of α-SMA also increased with the increase in fibrosis severity (Fig. 2B). Notably, during the severe stage, there was a significant difference in α-SMA protein expression between the normal and mild groups and between the severe group (Fig. 2C and D). However, no significant difference was observed between the mild and normal groups (Fig. 2C and D).

As shown in Fig. 2E–H, the protein abundance of αvβ3 increased with increasing fibrosis severity. Integrin αv and integrin β3 in the mild fibrosis group was slightly increase than that in the normal group, and they in the severe fibrosis group was significantly than that in the mild group.

3.3. Pathological examination and PET/CT imaging of ^{18}F–AlF-NOTA-RGD2

To accurately assess the fibrosis stages in the mini pigs, further pathological biopsies were performed. Fibrosis progression was scored according to the Metavir system. As illustrated in Fig. 3A, HE staining revealed fibrosis without portal vein bridging or with a moderate few septa, which was defined as mild liver fibrosis (Fig. 3A and B). Further analysis using SR staining revealed a significant increase in collagen deposition as fibrosis progressed (Fig. 3C). Statistical analysis revealed significant differences between the mild and normal groups in terms of collagen accumulation (Fig. 3D). Similarly, significant disparities were also observed between severe conditions and both normal and mild conditions, underscoring the extent of fibrotic changes across different stages of liver fibrosis (Fig. 3D).

In our bile duct ligation BDL model, as shown in Fig. 3E, images at the mild and severe stages were comparable. We also quantitatively assessed the images for radiotracer heat, as shown in Fig. 3F. In the BDL model, ^{18}F–AlF-NOTA-RGD2Al uptake increased from mild to severe fibrosis, indicating an increase in liver radioactivity. Compared to those in the control group, the radioactivity

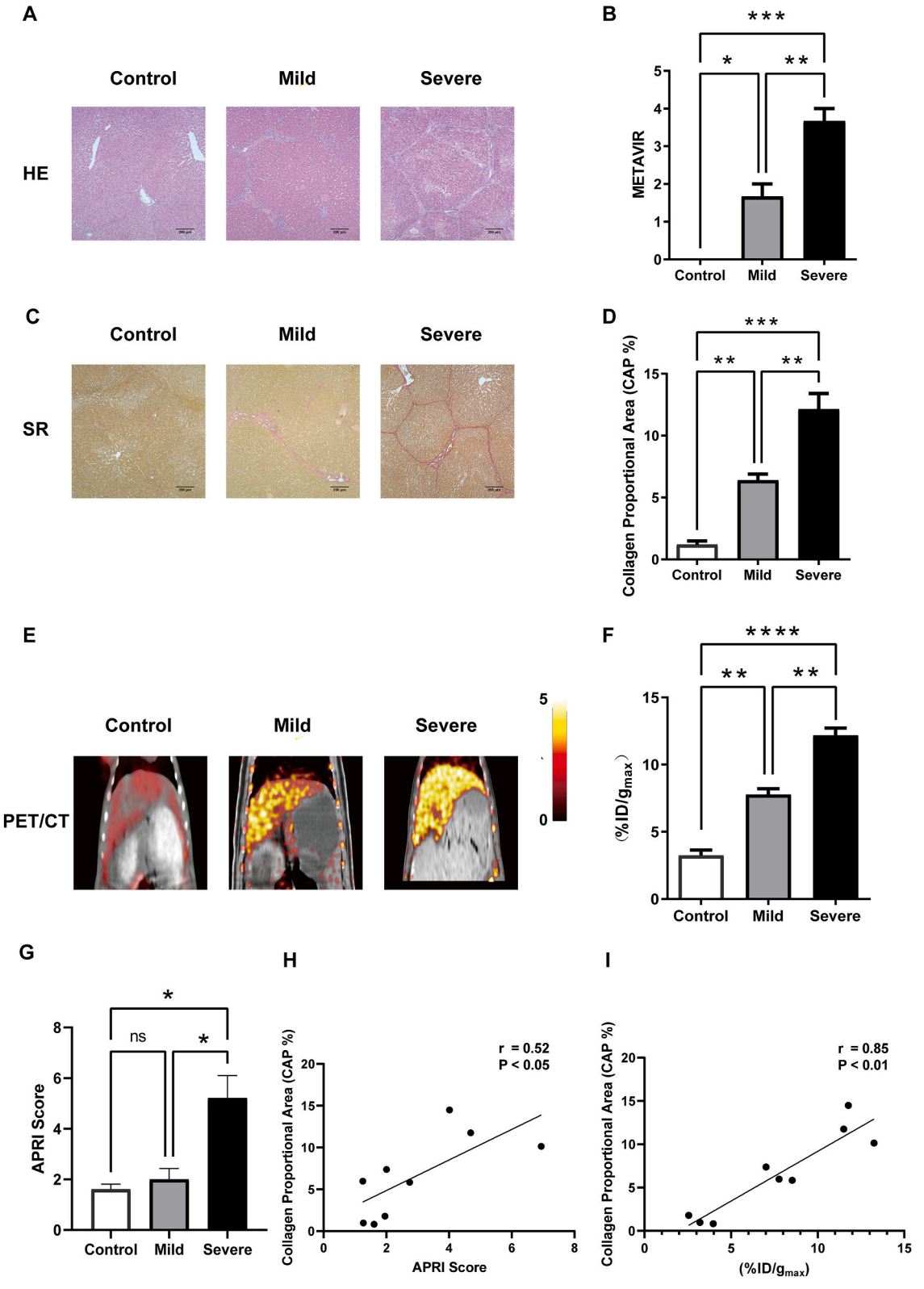

(caption on next page)

Fig. 3. Hepatic pathology and PET/CT imaging. (A) HE staining of the liver. Scale bar = 200 μm for all images. (B) METAVIR scoring of liver fibrosis. (C) SR staining of the liver. Scale bar = 200 μm for all images. (D) Propotional area of regenerated collagen (SR) stained. (E) PET/CT image. (F) Quantification of PET/CT data. (G) APRI score for liver fibrosis. (H) There was a linear correlation between the APRI score and the collagen propagation area, with a regression coefficient r = 0.52. (I) Linear correlation between the quantification of PET/CT and the collagen propagation area; regression coefficient r = 0.85. The data are expressed as the mean ± standard error (SEM) (n = 3 for each group). *P < 0.05, **P < 0.01, ***P < 0.001, ****P < 0.0001.

ratios in the livers of both mild and severe BDL pigs were significantly greater, corroborating that the PET imaging results are consistent with the pathological findings (Fig. 3F).

Compared with existing noninvasive approaches, we calculated the APRI score and found no significant difference between the normal and mild fibrosis groups, although there was a significant difference between the mild and severe fibrosis groups (Fig. 3G). Further analysis revealed that the APRI (Fig. 3H) and PET/CT (Fig. 3I) were positively correlated with the collagen proportional area, but the correlation of PET/CT was stronger than that of the APRI.

3.4. Mitochondrial reserve function

The function of hepatocytes reflects their functional state. The examination of glutathione revealed a decrease in both hepatic total glutathione content and glutathione levels as liver fibrosis progressed (Fig. 4A and B). Furthermore, a significant difference in the GSH/GSSG ratio was detected between the severe-stage group and both the normal-stage group and mild-stage group (Fig. 4C). This indicates a gradual deterioration of liver function as fibrosis progresses.

Furthermore, analysis of the mitochondrial Seahorse oxygen consumption curve provided insights into several key parameters: reserve capacity, ATP-linked oxygen consumption rate, nonmitochondrial respiration, and proton leakage (Fig. 4D). There was a significant decrease in the liver mitochondrial density in the tissue with the progression of fibrosis (Fig. 4E and F). Compared with that in patients with mild fibrosis, maximal respiration in patients with severe fibrosis was significantly lower (Fig. 4F). Notably, in severe liver fibrosis, there was a marked impairment in the mitochondrial reserve capacity of the mini pigs.

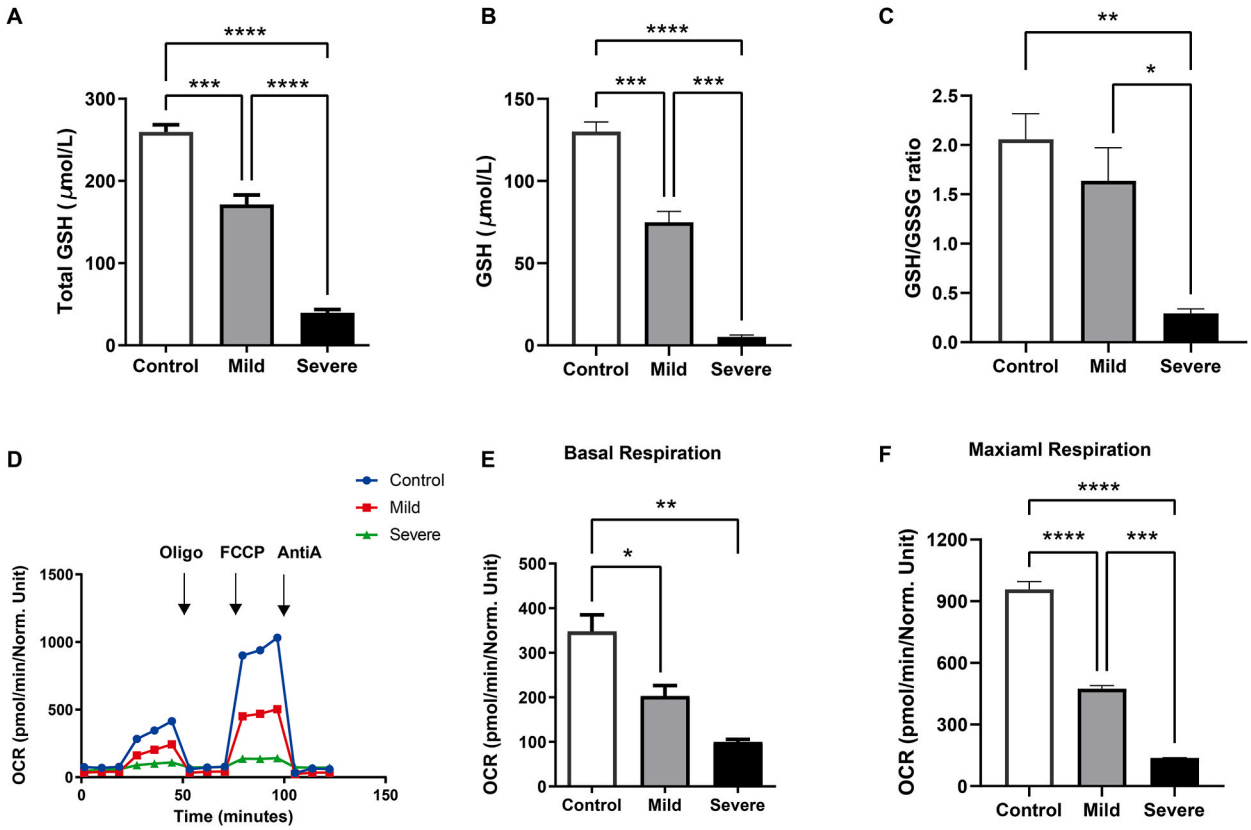

Fig. 4. Mitochondrial reserve function assessment. (A) Total glutathione (GSH). (B) GSH and (C) the glutathione (GSH)/GSSG ratio. (D) The oxygen consumption rate of the pigs. (E) Basal respiration and (F) maximal respiration of the oxygen consumption rate. The data are expressed as the mean ± standard error (SEM) (n = 3 for each group). *P < 0.05, **P < 0.01, ***P < 0.001, ****P < 0.0001.

4. Discussion

This study highlights the considerable promise of ^{18}F–AlF-NOTA-RGD2 PET/CT as a noninvasive diagnostic tool for the assessment of liver fibrosis stages in mini pigs. Notably, the differential uptake of 18F–AlF-NOTA-RGD2, which is correlated with the various stages of liver fibrosis, underlines the specificity of the probe for integrin αvβ3. This integrin plays a pivotal role in liver fibrogenesis and is upregulated during this process [6]. Such specificity distinctly sets this molecular imaging method apart from conventional imaging approaches, which typically lack the sensitivity required for early fibrosis detection.

This study also addresses the limitations of noninvasive markers, such as common hematological parameters, in distinguishing between the mild and normal stages of liver fibrosis. Although these markers can identify severe liver fibrosis, their effectiveness is less pronounced when differentiating between the initial stages of the disease, as demonstrated by parameters such as AST, ALP, and DBIL [21]. Despite these limitations, our research suggested that PET/CT could serve as a robust noninvasive alternative, complementing histopathological evaluations by providing quantitative insights into the extent of liver fibrosis.

An interesting aspect revealed by this study is the correlation between elevated liver enzyme levels and advanced stages of fibrosis, which is consistent with the literature [22]. However, these biochemical markers, while informative, often fall short in the precise staging of liver fibrosis [1]. This shortfall underscores the potential of combining 18F–AlF-NOTA-RGD2 PET/CT imaging with serum enzyme profiling to enhance the overall diagnostic accuracy, providing a more detailed assessment of liver health.

Although histopathological analysis continues to be the definitive standard for liver fibrosis staging, its invasive nature and associated patient risks limit its utility for frequent monitoring [21]. In contrast, the noninvasive nature of 18F–AlF-NOTA-RGD2 PET/CT facilitates ongoing monitoring of fibrosis progression, potentially reducing the need for regular biopsies and thereby minimizing patient discomfort and risk [23].

Considering the current paucity of quantitative diagnostic methods for liver fibrosis and building upon our team's previous research, we employed the ability of 18F-alfatide to specifically bind to αvβ3 integrin on activated hepatic stellate cells (aHSCs). The 18F-labeled radioactive tracer can detect fibrotic liver tissue, and PET/CT was used for imaging calculations. Concurrently, hydroxyproline quantification, Sirius red staining, and image analysis were performed on the liver tissue of animal models with different degrees of fibrosis, revealing the quantitative relationship between αvβ3 expression and the liver collagen content. Additionally, we explored the feasibility of 18F-Alfatide PET/CT imaging of the αvβ3 protein to evaluate liver mitochondrial function, aiming to accurately assess different degrees of liver fibrosis and reflect liver reserve function.

Furthermore, this study sheds light on mitochondrial dysfunction, identified through reduced mitochondrial enzyme activity, as a significant aspect of liver fibrosis [20]. This insight opens up new avenues for understanding the pathogenesis of liver fibrosis and positions mitochondrial impairment as a potential therapeutic target. The ability of 18F–AlF-NOTA-RGD2 PET/CT to indirectly assess mitochondrial function represents a promising new direction for research.

This study demonstrated that the correlation between PET/CT imaging and liver mitochondrial function provides new perspectives for evaluating liver health, which is especially relevant in the pre- and postsurgical setting. This correlation is vital because mitochondrial function is integral to energy metabolism and reflects the ability of the liver to recover postresection. Our results show that molecular probes can differentiate the degree of fibrosis at different stages. It would be a significant discovery if they could also evaluate mitochondrial function.

The implications of our findings extend beyond mere diagnostic utility; they underscore the potential of PET/CT as a predictive tool for assessing the risk and feasibility of liver surgeries. By providing a noninvasive means to gauge mitochondrial function, PET/CT imaging could help clinicians tailor their surgical approaches and postoperative care to the individual patient's liver function, enhancing recovery prospects and minimizing complications.

Additionally, integrating PET/CT metrics with conventional liver function tests could lead to more refined patient selection criteria for liver resection and enhance prognostic models [14]. Although these findings are promising, further investigations are needed to confirm their clinical applicability and to develop standardized protocols for incorporating PET/CT into liver surgery planning and postoperative care.

Furthermore, this study sheds light on mitochondrial dysfunction, identified through reduced mitochondrial enzyme activity, as a significant aspect of liver fibrosis [20]. This insight opens up new avenues for understanding the pathogenesis of liver fibrosis and positions mitochondrial impairment as a potential therapeutic target. The ability of 18F–AlF-NOTA-RGD2 PET/CT to indirectly assess mitochondrial function represents a promising new direction for research.

In conclusion, our study reaffirms the significant potential of 18F–AlF-NOTA-RGD2 PET/CT imaging in the noninvasive assessment of liver fibrosis, providing a valuable alternative to traditional diagnostic methodologies. These results could significantly influence patient management and treatment strategies for liver diseases, highlighting the necessity for longitudinal studies and human clinical trials to further validate and extend these findings.

Funding statement

This study was supported in part by the Sichuan Science and Technology Programme (grant number 2022YFS0090).

Data availability

Data will be made available upon request.

CRediT authorship contribution statement

Wenrui Liu: Writing – original draft, Investigation, Data curation, Conceptualization. **Hongwei Xu:** Methodology, Formal analysis. **Haili Zhang:** Methodology, Data curation. **Maodi Xie:** Resources, Methodology. **Yundi Liu:** Resources, Methodology, Investigation. **Li Wang:** Methodology, Resources. **Xiaoai Wu:** Writing – review & editing, Methodology. **Yinrui Feng:** Writing – review & editing, Writing – original draft, Project administration, Investigation. **Kefei Chen:** Writing – review & editing, Project administration, Funding acquisition, Conceptualization.

Declaration of competing interest

The authors declare that they have no known competing financial interests or personal relationships that could have appeared to influence the work reported in this paper.

Acknowledgments

The authors thank Ms. Hongge Wang and Mr. Bo Ma for assistance in animal care and surgery.

Appendix A. Supplementary data

Supplementary data to this article can be found online at https://doi.org/10.1016/j.heliyon.2024.e35502.

References

[1] L.Z. Kong, N. Chandimali, Y.H. Han, D.H. Lee, J.S. Kim, S.U. Kim, T.D. Kim, D.K. Jeong, H.N. Sun, D.S. Lee, T. Kwon, Pathogenesis, early diagnosis, and therapeutic management of alcoholic liver disease, Int. J. Mol. Sci. 20 (2019), https://doi.org/10.3390/ijms20112712.
[2] C.J. Parsons, M. Takashima, R.A. Rippe, Molecular mechanisms of hepatic fibrogenesis, J. Gastroenterol. Hepatol. 22 (2007) 79–84, https://doi.org/10.1111/j.1440-1746.2006.04659.x.
[3] P. Mathurin, A. Hadengue, R. Bataller, G. Addolorato, P. Burra, A. Burt, J. Caballeria, H. Cortez-Pinto, C.P. Day, E.H. Forrest, A. Gual, D.A. Leon, A. Lligoña, P. Jepsen, S. Mueller, G.P. Pageaux, T. Roskams, H.K. Seitz, F. Stickel, M. Thursz, S. Naveau, T. Morgan, F. Nevens, EASL clinical practical guidelines: management of alcoholic liver disease, J. Hepatol. 57 (2012) 399–420, https://doi.org/10.1016/j.jhep.2012.04.004.
[4] H. Han, H. Hu, Y.D. Xu, W.P. Wang, H. Ding, Q. Lu, Liver failure after hepatectomy: a risk assessment using the prepre-hepatectomy shear wave elastography technique, Eur. J. Radiol. 86 (2017) 234–240, https://doi.org/10.1016/j.ejrad.2016.11.006.
[5] P.J. Eddowes, M. Sasso, M. Allison, E. Tsochatzis, Q.M. Anstee, D. Sheridan, I.N. Guha, J.F. Cobbold, J.J. Deeks, V. Paradis, P. Bedossa, P.N. Newsome, Accuracy of FibroScan controlled attenuation parameter and liver stiffness measurement in assessing steatosis and fibrosis in patients with nonalcoholic fatty liver disease, Gastroenterology 156 (2019) 1717–1730, https://doi.org/10.1053/j.gastro.2019.01.042.
[6] T. Shao, Z. Chen, V. Belov, X. Wang, S.H. Rwema, V. Kumar, H. Fu, X. Deng, J. Rong, Q. Yu, L. Lang, W. Lin, L. Josephson, A.E. Samir, X. Chen, R.T. Chung, S. H. Liang, [18F]-Alfatide PET imaging of integrin αvβ3 for the non-invasive quantification of liver fibrosis, J. Hepatol. 73 (2020) 161–169, https://doi.org/10.1016/j.jhep.2020.02.018.
[7] X. Bao, M.W. Wang, J.M. Luo, S.Y. Wang, Y.P. Zhang, Y.J. Zhang, Optimization of early response monitoring and prediction of cancer antiangiogenesis therapy via noninvasive PET molecular imaging strategies of multifactorial bioparameters, Theranostics 6 (2016) 2084–2098, https://doi.org/10.7150/thno.13917.
[8] T. Lan, C. Li, G. Yang, Y. Sun, L. Zhuang, Y. Ou, H. Li, G. Wang, T. Kisseleva, D. Brenner, J. Guo, Sphingosine kinase 1 promotes liver fibrosis by preventing miR-19b-3p-mediated inhibition of CCR2, Hepatology 68 (2018) 1070–1086, https://doi.org/10.1002/hep.29885.
[9] Z.H. Jin, T. Furukawa, T. Ohya, M. Degardin, A. Sugyo, A.B. Tsuji, Y. Fujibayashi, M.R. Zhang, T. Higashi, D. Boturyn, P. Dumy, T. Saga, 67Cu-Radiolabeling of a multimeric RGD peptide for α v β 3 integrin-targeted radionuclide therapy: stability, therapeutic efficacy, and safety studies in mice, Nucl. Med. Commun. 38 (2017) 347–355, https://doi.org/10.1097/MNM.0000000000000646.
[10] M.B. Haskali, D. Denoyer, W. Noonan, C. Culinane, C. Rangger, N. Pouliot, R. Haubner, P.D. Roselt, R.J. Hicks, C.A. Hutton, Sulfonation of tyrosine as a method to improve biodistribution of peptide-based radiotracers: novel 18F-labeled cyclic RGD analogues, Mol. Pharm. 14 (2017) 1169–1180, https://doi.org/10.1021/acs.molpharmaceut.6b01062.
[11] M. Prodeau, E. Drumez, A. Duhamel, E. Vibert, O. Farges, G. Lassailly, J.Y. Mabrut, J. Hardwigsen, J.M. Régimbeau, O. Soubrane, R. Adam, F.R. Pruvot, E. Boleslawski, An ordinal model to predict the risk of symptomatic liver failure in patients with cirrhosis undergoing hepatectomy, J. Hepatol. 71 (2019) 920–929, https://doi.org/10.1016/j.jhep.2019.06.003.
[12] J. Meyer, A. Balaphas, C. Combescure, P. Morel, C. Gonelle-Gispert, L. Bühler, Systematic review and meta-analysis of thrombocytopenia as a predictor of post-hepatectomy liver failure, Hpb 21 (2019) 1419–1426, https://doi.org/10.1016/j.hpb.2019.01.016.
[13] C.C.N. Chong, G.L.H. Wong, A.W.H. Chan, V.W.S. Wong, A.K. wai Fong, Y.S. Cheung, J. Wong, K.F. Lee, S.L. Chan, P.B.S. Lai, H.L.Y. Chan, Liver stiffness measurement predicts high-grade post-hepatectomy liver failure: a prospective cohort study, J. Gastroenterol. Hepatol. 32 (2017) 506–514, https://doi.org/10.1111/jgh.13503.
[14] N. Guo, L. Lang, W. Li, D.O. Kiesewetter, H. Gao, G. Niu, Q. Xie, X. Chen, Quantitative analysis and comparison study of [18f]alf-nota-prgd2, [18f]fpprgd2 and [68ga]ga-nota-prgd2 using a reference tissue model, PLoS One 7 (2012) 1–9, https://doi.org/10.1371/journal.pone.0037506.
[15] M. Mammen, S.K. Choi, G.M. Whitesides, Polyvalent interactions in biological systems: implications for design and use of multivalent ligands and inhibitors, Angew. Chem. Int. Ed. 37 (1998) 2754–2794, https://doi.org/10.1002/(sici)1521-3773(19981102)37:20<2754::aid-anie2754>3.0.co;2-3.
[16] D.M. Goldenberg, R.M. Sharkey, W.J. Mcbride, O.C. Boerman, Al18F: a new standard for radiofluorination, J. Nucl. Med. 54 (2013) 1170, https://doi.org/10.2967/jnumed.113.125245.
[17] Y. Cui, H. Liu, S. Liang, C. Zhang, W. Cheng, The Feasibility of 18 F-AlF-NOTA-PRGD2 PET/CT for Monitoring Early Response of Endostar Antiangiogenic Therapy in Human Nasopharyngeal Carcinoma Xenograft Model Compared with F-FDG, vol. 7 (n.d.).
[18] Y. Feng, W. Liu, T. Ba, Z. Luo, Y. Ma, G. Tang, Y.J. Kang, Zinc-glutathione in Chinese Baijiu prevents alcohol-associated liver injury, Heliyon 9 (2023) e13722, https://doi.org/10.1016/j.jnutbio.2021.108803.
[19] C. Xie, L. Wan, C. Li, Y. Feng, Y.J. Kang, Selective suppression of M1 macrophages is involved in zinc inhibition of liver fibrosis in mice, J. Nutr. Biochem. 97 (2021) 108802, https://doi.org/10.1016/j.jnutbio.2021.108802.

[20] K.S. McCommis, A. Kovacs, C.J. Weinheimer, T.M. Shew, T.R. Koves, O.R. Ilkayeva, D.R. Kamm, K.D. Pyles, M.T. King, R.L. Veech, B.J. DeBosch, D.M. Muoio, R. W. Gross, B.N. Finck, Nutritional modulation of heart failure in mitochondrial pyruvate carrier–deficient mice, Nat. Metab. 2 (2020) 1232–1247, https://doi.org/10.1038/s42255-020-00296-1.

[21] F. Segovia-Miranda, H. Morales-Navarrete, M. Kücken, V. Moser, S. Seifert, U. Repnik, F. Rost, M. Brosch, A. Hendricks, S. Hinz, C. Röcken, D. Lütjohann, Y. Kalaidzidis, C. Schafmayer, L. Brusch, J. Hampe, M. Zerial, Three-dimensional spatially resolved geometrical and functional models of human liver tissue reveal new aspects of NAFLD progression, Nat. Med. 25 (2019) 1885–1893, https://doi.org/10.1038/s41591-019-0660-7.

[22] C. Moreno, S. Mueller, G. Szabo, Non-invasive diagnosis and biomarkers in alcohol-related liver disease, J. Hepatol. 70 (2019) 273–283, https://doi.org/10.1016/j.jhep.2018.11.025.

[23] T. Vita, D.J. Murphy, M.T. Osborne, N.S. Bajaj, A. Keraliya, S. Jacob, A.J.D. Martinez, A. Nodoushani, P. Bravo, J. Hainer, C.F. Bibbo, M.L. Steigner, V. R. Taqueti, H. Skali, R. Blankstein, M.F. Di Carli, S. Dorbala, Association between nonalcoholic fatty liver disease at CT and coronary microvascular dysfunction at myocardial perfusion PET/CT, Radiology 291 (2019) 330–337, https://doi.org/10.1148/radiol.2019181793.